

Structures of complete extracellular assemblies of type I and type II Oncostatin M receptor complexes

Received: 6 December 2023

Accepted: 31 October 2024

Published online: 12 November 2024



Yi Zhou , Panayiotis E. Stevis, Jing Cao, George Ehrlich, Jennifer Jones, Ashique Rafique , Mark W. Sleeman, William C. Olson & Matthew C. Franklin 

Oncostatin M (OSM) is a unique Interleukin 6 (IL-6) family cytokine that plays pivotal roles in numerous biological events by signaling via two types of receptor complexes. While type I OSM receptor complex is formed by glycoprotein 130 (gp130) heterodimerization with Leukemia Inhibitory Factor receptor (LIFR), type II OSM receptor complex is composed of gp130 and OSM receptor (OSMR). OSM is an important contributor to multiple inflammatory diseases and cancers while OSM inhibition has been shown to be effective at reducing symptoms, making OSM an attractive therapeutic target. Using cryogenic electron microscopy (cryo-EM), we characterize full extracellular assemblies of human type I OSM receptor complex and mouse type II OSM receptor complex. The juxtamembrane domains of both complexes are situated in close proximity due to acute bends of the receptors. The rigid N-terminal extension of OSM contributes to gp130 binding and OSM signaling. Neither glycosylation nor pro-domain cleavage of OSM affects its activity. Mutagenesis identifies multiple OSM and OSMR residues crucial for complex formation and signaling. Our data reveal the structural basis for the assemblies of both type I and type II OSM receptor complexes and provide insights for modulation of OSM signaling in therapeutics.

Interleukin 6 (IL-6) family cytokines, including Oncostatin M (OSM), IL-6, Leukemia Inhibitory Factor (LIF), Ciliary Neurotrophic Factor (CNTF), Cardiotrophin Like Cytokine Factor 1 (CLCF1), IL-11, and IL-27, are actively involved in regulation of various cellular processes including immune response, inflammation, metabolism, embryonic development, neuronal and liver regeneration, and hematopoiesis^{1,2}. These cytokines all adopt a canonical four-helix bundle configuration comprising of four helices (termed helices A to D) and three loop regions (termed AB, BC, and CD loops). They also share three conserved receptor binding epitopes on the surface (termed Sites 1–3). Typically, Site 2 is bound by the shared receptor glycoprotein 130 (gp130) while Site 3 is occupied by a second gp130 molecule or another ‘tall’ signaling receptor, such as LIF receptor (LIFR) and OSM receptor

(OSMR). Site 1 may be bound by a non-signaling alpha receptor or remain unoccupied³. Upon assembly of the cytokine-receptor complexes on the cell membrane, various intracellular signaling events are initiated via activation of the Janus kinase/signal transducer and activator of transcription (JAK/STAT) proteins, which could further activate downstream signaling cascades, including the phosphoinositide 3-kinase/protein kinase B (PI3K/Akt) and the mitogen-activated protein kinase (MAPK) pathways^{4–8}.

Human OSM (hOSM) is a unique member of the IL-6 family cytokines due to its ability to signal via two types of receptor complexes: type I receptor complex comprised of hOSM, human gp130 (hgp130), and human LIFR (hLIFR), and type II receptor complex formed by hOSM, hgp130, and human OSMR (hOSMR)⁹. In addition, it

is the only IL-6 family membrane with a C-terminal pro-domain. Full-length hOSM contains 227 amino acids (termed ‘hOSM_long’ in this paper). Proteolytic cleavage can remove the 31 amino acids pro-domain at the C-terminus to yield a short form hOSM protein with 196 amino acids (termed ‘hOSM_short’ in this paper)¹⁰. The pro-domain of hOSM has been proposed to enhance hOSM binding to extracellular matrix in vivo, which may help to maintain a prolonged hOSM signaling and lead to chronic inflammation¹¹. hOSM serves as an important regulator of hematopoiesis, adipogenesis, osteogenesis, wound healing, and heart remodeling upon acute and chronic injury^{12,13}. It has been shown to contribute to multiple inflammatory diseases such as inflammatory bowel disease, arthritis, lung and skin disease, cardiovascular disease, COVID-19, as well as inflammatory pruritus^{10,14}. The disorder of hOSM signaling has also been implicated in several cancer types^{10,15}. Notably, the inhibition of hOSM signaling has been reported to be effective at treating these diseases or reducing symptoms, making hOSM a promising therapeutic target¹⁰.

hOSM is most closely related to human LIF (hLIF) in structure, function, and gene origination^{16,17}. The genes of these two cytokines are derived from the same ancestral gene via gene duplication^{18,19}, and retain structural similarity to each other despite low sequence identity. Because of this similarity, hOSM and hLIF can both signal through hgp130 heterodimerization with hLIFR, albeit via different assembly mechanisms: hLIF binds to hLIFR first before recruiting hgp130, while hOSM first interacts with hgp130 and then recruits hLIFR^{9,13,20}. Alternatively, hOSM is able to recruit hOSMR instead of hLIFR after binding to hgp130 to form the type II receptor complex^{9,21}. hOSM has a large unique helical loop between helices B and C that is not observed in hLIF. It has been proposed that the bulky BC loop of hOSM might modulate the interactions with hLIFR or hOSMR at Site 3 and lead to higher affinity of hOSM to hgp130 than to hLIFR or hOSMR¹³. As in human, the dual-receptor activation of OSM has also been identified in rat²². In contrast, mouse OSM (mOSM) primarily functions via type II receptor complex by activating mouse gp130 (m gp130) and mouse OSMR (mOSMR) since the binding affinity of mOSM to mouse LIFR (mLIFR) is very low^{23–26}. Several functional studies have suggested divergences in hOSM- and mOSM-mediated interactions with corresponding receptors and the lack of cross-species activities: hOSM can activate mLIFR but not mOSMR, whereas mOSM can signal via neither hLIFR nor hOSMR^{22,27}. Additionally, the AB loop of OSM has been shown to play a critical role in both activating OSMR and driving species-specific signaling in human and mouse^{23,28}.

Unlike most other IL-6 family cytokine receptor complexes which are well characterized structurally^{3,29–33}, the architectures of both type I and type II OSM receptor complexes remain elusive. Although the crystal structure of hOSM was determined over two decades ago¹⁷, and the OSM-LIFR/OSMR interactions were recently predicted by molecular dynamics simulations^{34,35}, there is no experimental structural information for OSM in complex with either of its receptors, likely due to high flexibility and instability of the OSM-receptor complexes.

Here, we determine cryogenic electron microscopy (cryo-EM) structures of human type I OSM receptor complex (hOSM/hgp130/hLIFR complex) and mouse type II OSM receptor complex (mOSM/mgp130/mOSMR complex) to sub-4 Å resolution using full extracellular domains of the receptors. The receptors all adopt a characteristic acute bent conformation between the third to the last and the second to the last domains of the extracellular region that can bring the juxtamembrane domains of both complexes into close proximity (~25 Å). This geometry is also seen in other IL-6 family cytokine receptor complexes and is important for initiation of downstream signaling^{3,32}. The rigid N-terminal extension of hOSM can function to boost hgp130 binding and hOSM signaling. We also identify a number of OSM and OSMR residues critical for complex formation and signaling and confirmed that the glycosylation and pro-domain cleavage of OSM do not affect its activity in vitro. Collectively,

our studies reveal similarities and differences in the assembly of type I and type II OSM receptor complexes, identify antagonistic mutations on both OSM and OSMR, and provide valuable insights for developing treatments to target OSM-mediated signaling pathways.

Results

Cryo-EM structure of human type I OSM receptor complex (hOSM/hgp130/hLIFR complex)

Human type I OSM receptor complex is composed of hOSM, hgp130 and hLIFR (Fig. 1a). Although key OSM residues involved in binding to gp130 at Site 2 and LIFR at Site 3 have been largely identified by several mutagenesis and biochemical studies^{17,23,28,36,37}, the overall architecture of the complex remains unknown. We therefore reconstituted this complex using full extracellular domains of hgp130 and hLIFR³, and a short form hOSM protein without the C-terminal pro-domain. The complex was characterized by single-particle cryo-EM, showing 2D class averages with multiple orientations and clear secondary structural features (Fig. 1b). A density map with a global resolution of 3.59 Å (Map 1) was obtained (Supplementary Fig. 1a–e, Fig. 1c). This map has well resolved density around the interaction core region, including hOSM, hgp130 D2D3, and hLIFR D3D4, permitting manual model building and real space refinement of this region for the characterization of interaction details at the two ligand-receptor binding interfaces (Fig. 1d, Supplementary Fig. 1e). N-linked glycan densities are observed on all three components around the assembly core area, including hOSM (N100), hgp130 (N131, N157, N227), and hLIFR (N303, N407, N426), although none of the glycans is directly involved in interactions (Fig. 1d).

To examine whether hOSM glycosylation and its pro-domain affect its activity, we performed STAT3 luciferase reporter assay in human IMR32 cells, which respond to hOSM but not mouse OSM (mOSM) (Supplementary Fig. 2a), confirming that mOSM cannot signal through human receptors²⁷. Notably, hOSM proteins derived from HEK293 (glycosylated) and *E. coli* (non-glycosylated), both in short form without the pro-domain (hOSM_short), show similar activity (Supplementary Fig. 3a). In addition, we purified long form hOSM protein with the pro-domain (hOSM_long) from HEK293 cells. Notably, a weak dimer band was observed on the SDS-PAGE gel under non-reduced condition but not under reduced condition (Supplementary Fig. 4a), indicating some disulfide bond-mediated dimerization of hOSM in vitro. The detection of the Myc tag at the C-terminal end of the proteins confirmed that the pro-domain was not cleaved during protein expression and secretion (Supplementary Fig. 4b). As shown in Supplementary Fig. 3a, long form hOSM shows no significant difference at activating STAT3. These data together indicate that hOSM glycosylation and its pro-domain both have no major effect on hOSM activity in vitro.

Due to the flexible nature of the ‘tall’ signaling receptors, the distal ends of hgp130 and hLIFR in Map 1 have lower resolution (Supplementary Fig. 1c). Specifically, the membrane-proximal domains of the two receptors have quite fragmented density, likely due to high heterogeneity induced by flexibility of these regions. A subset of particles was further identified by heterogeneous refinement, yielding another map (Map 2) with lower global resolution (3.99 Å) but improved density for the receptor juxtamembrane domains (Fig. 1e, Supplementary Fig. 1a, f, g). The second map was used for placement and rigid-body fitting of AlphaFold³⁸ models for the receptor distal domains to generate a complete model for extracellular assembly of the type I hOSM receptor complex (Fig. 1f, g). Like LIF, CNTF, and CLCF1 signaling complexes³, the acute bends of hgp130 at D4D5 and hLIFR at D6D7 bring the bottom centers of the receptor juxtamembrane domains of this complex into close proximity (~26 Å apart) (Fig. 1g), which is an important geometry for the initiation of downstream signaling. To rule out the possibility that the bent conformation of the receptor juxtamembrane domains observed in our structure might be induced by the

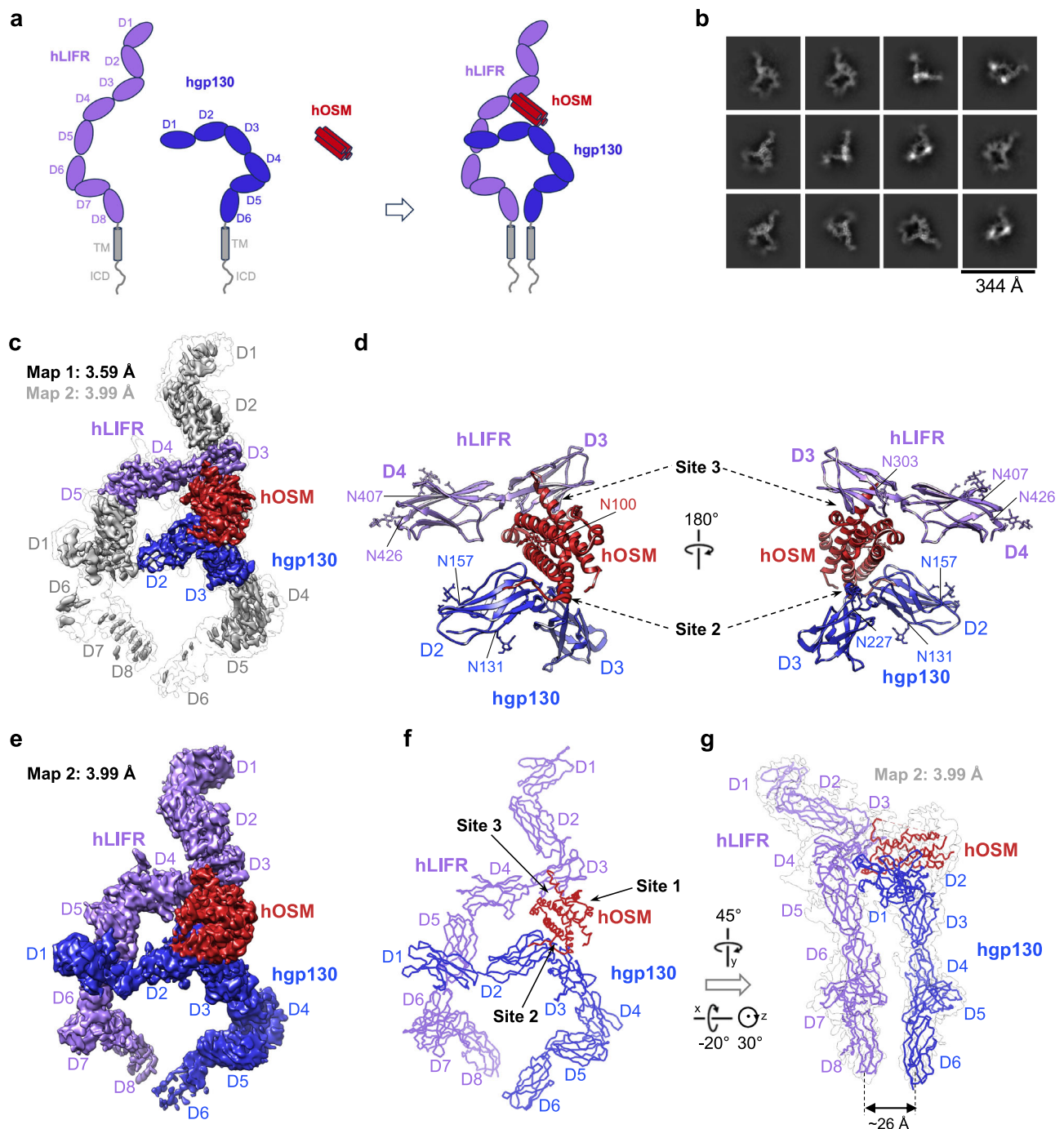


Fig. 1 | Cryo-EM structure of human type I OSM receptor complex (hOSM/hgp130/hLIFR complex). **a** Schematic representation of human OSM/gp130/LIFR complex assembly, with hLIFR, hgp130, and hOSM colored in purple, blue, and dark red, respectively. Transmembrane (TM) region and intracellular domains (ICD) of hLIFR and hgp130 were excluded from the constructs and were colored in gray. **b** Representative 2D class averages of human OSM/gp130/LIFR complex with full extracellular assembly. **c** 3.59 Å cryo-EM density map (Map 1) was overlaid with transparent Map 2 (3.99 Å). The assembly core regions of Map 1 (hOSM, hgp130 D2D3, and hLIFR D3D4) were colored as in (a) while the remaining parts of the map

were colored in gray. **d** The atomic model of human OSM/gp130/LIFR complex assembly core region (hOSM, hgp130 D2D3, and hLIFR D3D4) manually built and refined against Map 1 was shown in cartoon form in two orientations. Glycosylation sites in this region were highlighted in stick representation. **e** 3.99 Å cryo-EM density map (Map 2) of human OSM/gp130/LIFR complex colored as in (a). **f** Model of complete extracellular assembly of human OSM/gp130/LIFR complex depicted in C-alpha ribbon traces. **g** Side view of the full extracellular assembly model in transparent Map 2. Approximate distances between the bottom centers of hLIFR and hgp130 juxtamembrane domains is estimated.

absence of transmembrane (TM) domain and intracellular domain (ICD), we purified detergent-solubilized full length hgp130 and characterized its cryo-EM structure with the aid of an anti-gp130 antibody B-S12 Fab (Supplementary Fig. 5a–c). In some 2D class average views, a circle with a bright dot in the center is observed, likely representing the

TM of hgp130 embedded in the detergent micelle (Supplementary Fig. 5b). However, only the extracellular domain (ECD) of hgp130 is resolved in the 3D reconstruction due to high flexibility of the TM and ICD relative to the ECD (Supplementary Fig. 5c). The characteristic bend between D4 and D5 is also observed in full length hgp130,

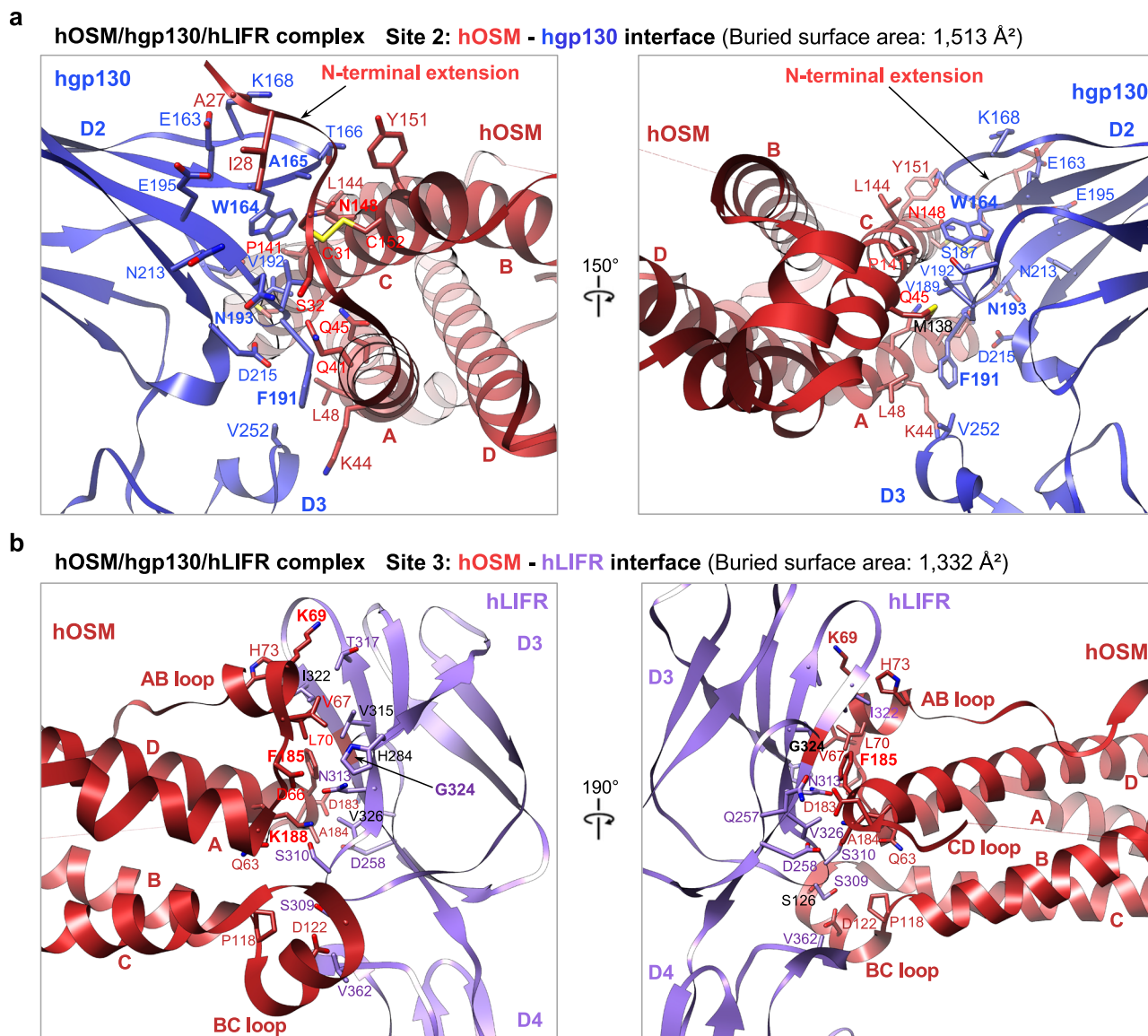


Fig. 2 | Structural basis for the assembly of human type I OSM receptor complex (hOSM/hgp130/hLIFR complex). Close-up views of hOSM-hgp130 Site 2 (**a**) and hOSM-hLIFR Site 3 (**b**) binding interfaces shown in cartoon form, with residues involved in binding shown in stick representation. Each interface was shown in two

orientations. All-atom real-space refined model of the complex interaction core region shown in Fig. 1d was used for the analysis. Buried surface areas of the two binding interfaces were calculated by PDBEPIA.

suggesting that the truncation of hgp130 TM and ICD does not affect its ECD conformation. In addition, there is no major conformational change of hgp130 ECD upon binding to hOSM (Supplementary Fig. 5d).

The architecture of hOSM-hgp130 Site 2 interface

Analogous to the way gp130 engages CNTF, CLCF1, LIF, IL-11, and IL-6 at Site 2^{3,29,32,33,39,40}, the Site 2 binding interface of type I hOSM complex is formed by the cytokine-binding homology region (CHR, D2D3) of hgp130 engaging hOSM helices A and C, which buries a total surface area of 1,513 Å² (Figs. 1d, f, 2a). As shown in Fig. 2a, F191 of hgp130 serves as an aromatic anchor by inserting into a hydrophobic pocket formed by L48 and the hydrophobic portions of Q41, K44, and Q45 on helix A of hOSM (residue numbering of all proteins described in this paper is based on their UniProt sequences). Therefore, hgp130 F191 contributes the largest fraction of buried surface area (120 Å²) at the interface from the receptor side, corroborating the notion that hgp130 positions 189–192 are essential for OSM binding³⁶. N193 and D215 of hgp130 further enhance the engagement with helix A by

coordinating with hOSM Q41 through hydrophilic interactions at the center of the interface. The importance of hOSM Q41 and Q45 in hgp130 binding has been supported by previous alanine-scanning mutagenesis¹⁷. Furthermore, a purified short form hOSM mutant in which these two glutamine residues are substituted by bulky tryptophane residues (Q41W/Q45W, Supplementary Fig. 4c) shows nearly undetectable activity in human IMR32 cells (Fig. 3a). Consistently, this mutant does not bind to hgp130 in vitro (Fig. 3b, Supplementary Fig. 6). hOSM helix C is held in position primarily by hgp130 W164 and V192, which capture the middle portion of the helix through extensive interactions with G145, N148, and N149 of hOSM (Supplementary Fig. 7). Specifically, hOSM G145 in the middle of helix C is tightly packed against hgp130 W164 and V192. The substitution of hOSM G145 with an alanine or a bulkier residue tyrosine abolishes hOSM signaling^{17,37}, presumably because there is not sufficient space to accommodate a bulky side chain at the binding interface. The critical role of hOSM N149 has also been corroborated by alanine substitution¹⁷. While the N148A mutation only moderately reduces

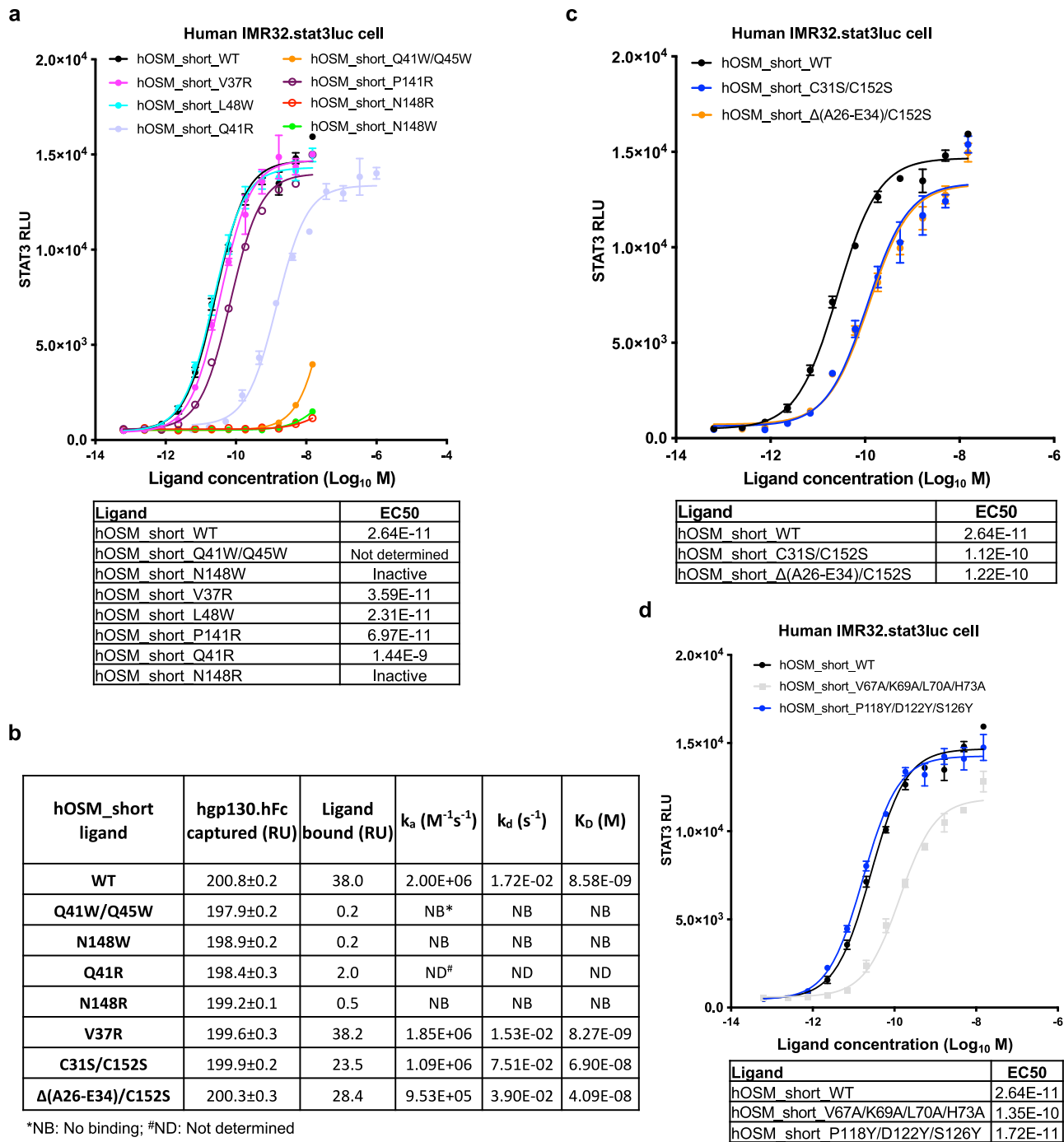


Fig. 3 | Structure based mutagenesis studies identified several antagonistic mutants of hOSM. a STAT3-luciferase reporter assay was performed in IMR-32 cells after treating the cells with short form hOSM WT and seven mutant proteins with mutations at Site 2. Half maximal effective concentration (EC50) for each protein was shown in the table. The data shown are representative of 5 independent experiments with similar results. Error bars represent standard deviations. RLU: relative luminescence units. **b** Comparison of association rate constant (k_a), dissociation rate constant (k_d), and equilibrium dissociation constant (K_D) for hgp130.hFc binding to hOSM WT and seven variants determined by Surface plasmon resonance. The data shown are representative of 2 independent experiments

with similar results. **c** STAT3-luciferase reporter assay was performed in IMR-32 cells after treating the cells with short form hOSM WT and two mutants with mutations at the N-terminal extension. EC50 for each protein was shown in the table. The data shown are representative of 5 independent experiments with similar results. Error bars represent standard deviations. **d** STAT3-luciferase reporter assay was performed in IMR-32 cells after treating the cells with short form hOSM WT and two mutants with mutations at Site 3. EC50 for each protein was shown in the table. The data shown are representative of 5 independent experiments with similar results. Error bars represent standard deviations. Source data are provided as a Source Data file.

hOSM activity^{17,37}, we found that replacing N148 with tryptophane (N148W, Supplementary Fig. 4c) completely eliminates hOSM binding to hgp130 (Fig. 3b, Supplementary Fig. 6) and abolishes STAT3 activation (Fig. 3a). We further attempted to introduce some mutations that may boost hOSM activity, including V37R, Q41R, L48W, P141R, and

N148R (Supplementary Fig. 4c), in the hope of introducing new electrostatic interaction, cation- π interaction, or strong hydrophobic interaction to enhance binding to hgp130. However, V37R, L48W, and P141R do not substantially affect hOSM signaling, while Q41R and N148W largely and completely inhibit hOSM activity, respectively

(Fig. 3a). Accordingly, the Q41R and N148R mutations result in nearly undetectable and totally eliminated hgp130 binding, respectively, whereas the V37R mutation has no effect on binding to hgp130 (Fig. 3b, Supplementary Fig. 6).

While hOSM binding to hgp130 is predominantly mediated by D2 of hgp130, V252 from D3 can serve to stabilize the binding via interactions with L48 and K44 at the middle of hOSM helix A (Fig. 2a). Notably, hgp130 V252 is also involved in binding to CNTF, CLCF1, LIF and IL-6³.

The rigid N-terminal extension of hOSM contributes to hgp130 binding and hOSM signaling

hOSM has a rigid N-terminal extension (residues A26–E34) preceding helix A (Fig. 2a). This extension is tethered to helix C by a disulfide bond formed by C31 and C152, and extends around the surface of hgp130 D2, introducing additional interactions at the Site 2 interface. The engagement of four residues (A27, I28, C31, and S32) in this region with several hgp130 residues along the extension path contributes ~30% of buried surface area from the ligand side, which might serve to improve hOSM Site 2 affinity to gp130 and lead to the alpha receptor independence of hOSM for signaling. Intriguingly, similar N-terminal extension is also observed in LIF that signals in the absence of a non-signaling alpha receptor, but not in other cytokines of this family that requires alpha receptors for signaling³.

To test whether the rigid N-terminal extension of hOSM is indeed important for signaling, we purified two short form hOSM variants: one variant with the C31–C152 disulfide bond being eliminated by replacing the two cysteines with serines (C31S/C152S), and another variant with the N-terminal extension (residues A26–E34) truncation along with the C152S mutation so as to prevent intermolecular disulfide bond formation (Δ (A26–E34)/C152S) (Supplementary Fig. 4d). We hypothesized that removal of the C31–C152 disulfide bond may lead to increased flexibility of the N-terminal extension, which would decrease hOSM affinity to hgp130 and hence impair the signaling, while truncation of the entire N-terminal extension may have similar consequences. As expected, the two variants both demonstrate reduced efficacy (maximum effect) with ~4–5 fold lower potency (EC₅₀) compared with WT hOSM (Fig. 3c). We next utilized Surface plasmon resonance (SPR) to directly measure the kinetics of these hOSM proteins binding to hgp130 immobilized on the sensor chip surface via its hFc tag. Consistently, WT hOSM (K_D : 8.58 nM) shows ~5–8 fold higher affinity to hgp130 than the C31S/C152S variant (K_D : 69.0 nM) and the Δ (A26–E34)/C152S variant (K_D : 40.9 nM) (Fig. 3b, Supplementary Fig. 6). Compared with WT hOSM, both variants demonstrate lower association rate (k_a) and higher dissociation rate (k_d), suggesting that the rigid N-terminal extension of hOSM contributes to the recruitment of hgp130 at Site 2 and serves to stabilize the binding. Variant C31S/C152S shows the fastest dissociation, likely because its N-terminal extension is floppy without being tethered to helix C by the C31–C152 disulfide bond, which might have destabilized the binding. Notably, the sensorgram curves of variant Δ (A26–E34)/C152S do not fully reach baseline at the dissociation stage (Supplementary Fig. 6), probably due to higher percentage of dimer species in this sample that may affect the interactions (Supplementary Fig. 4d). Collectively, these data suggest that the rigid N-terminal extension of hOSM could function to improve the binding affinity to hgp130 at Site 2 and boost hOSM signaling, especially at relatively low ligand concentration.

The architecture of hOSM–hLIFR Site 3 interface

The Site 3 interface has a total buried surface area of 1,332 Å² and is formed by the posterior end of hOSM four-helix bundle docking onto the saddle-shaped LIFR Ig-like domain D3 (Figs. 1d, f, 2b), largely mimicking the way CNTF, CLCF1, and LIF engage LIFR³. The binding is primarily mediated by hOSM helix D and AB loop, with BC loop making additional contact with V362 in the N-terminal loop of LIFR D4

(Fig. 2b). The binding interface is centered around F185 and K188 in the evolutionarily conserved FXXK motif at the N-terminus of hOSM helix D, which is extended through the packing of the two short helices in AB and BC loops against LIFR D3 and D3/D4, respectively. The aromatic ring of hOSM F185 serves as a critical binding anchor by coordinating with N313, V315, I322, and V326 of hLIFR and making a π -stacking against the peptide bond of hLIFR G324. Another anchor, hOSM K188, further improves the binding through hydrogen bond interactions with S310 and N313 of hLIFR. Corroborating our observations, alanine substitutions of hOSM F185 and K188 have been shown to abolish the binding of hOSM to hLIFR¹⁷. A cluster of residues in the AB loop (G64, D66, V67, K69, L70, H73) make extensive interactions with a patch of residues in the N-terminal end of hLIFR D3 (H284, S310, N313, V315, T317, I322), which accounts for up to ~42% of buried surface area of hOSM at the interface. Consistently, alanine substitutions of four residues in hOSM AB loop (V67A/K69A/L70A/H73A) reduce both the potency and efficacy of the cytokine substantially (Fig. 3d). Specifically, K69 on the short helix of hOSM AB loop is coordinated by the backbone of a loop in the N-terminal end of hLIFR D3 through hydrogen bond formation. Notably, at equivalent location of hLIFR, there is also a lysine residue (K80) that engages hLIFR backbone in a similar manner³. In mouse OSM (mOSM), this lysine residue is replaced by a smaller and oppositely charged aspartic acid (D66) residue (Supplementary Fig. 8), which might be one reason why mOSM fails to bind and activate hLIFR²³. In contrast, hOSM can cross-react with mLIFR similarly to hLIFR⁴¹, likely because hLIFR residues critical for hOSM binding are largely conserved or similar in mLIFR (Supplementary Fig. 9). In order to identify potential agonistic mutations at Site 3, we tried to mutate three hLIFR-contacting residues in hOSM BC loop (P118Y/D122Y/S126Y, Supplementary Fig. 4c). However, these mutations have no impact on hOSM activity (Fig. 3d).

Cryo-EM structure of mouse type II OSM receptor complex (mOSM/mgp130/mOSMR complex)

Besides binding to LIFR, OSM can also bind to OSMR at Site 3 to form the type II receptor complex (Fig. 4a). Our initial attempts to solve the structure of human type II OSM receptor complex (hOSM/hgp130/hOSMR complex) were not successful since we could only observe hOSM–hgp130 sub-complex on the EM grid. Alternatively, we characterized mouse type II receptor complex by cryo-EM using full ectodomains of mgp130 and mOSMR, and a recombinant mOSM protein. We were able to observe intact mOSM/mgp130/mOSMR complex particles with different orientations (Fig. 4b). We obtained a cryo-EM map (Map 1) with a global resolution of 3.46 Å (Supplementary Fig. 10a–e, Fig. 4c). As with the hOSM type I receptor complex, this map's higher resolution around the assembly core region (mOSM, mgp130 D2D3, and mOSMR D2D3) permitted manual model building and real-space refinement of this region (Fig. 4c, d, Supplementary Fig. 10e), while density at the receptor distal domains was weaker due to high flexibility (Supplementary Fig. 10c). Adjacent to the assembly core area, multiple N-linked glycans were identified on mgp130 (N131, N157, N225) and mOSMR (N162, N239, N271, M304, N323), although none of the glycans directly contributes to the binding (Fig. 4d).

In our structural study, we utilized a short form mOSM protein derived from *E. coli*, which lacks glycosylation and the C-terminal pro-domain. To investigate whether mOSM glycosylation and its pro-domain affect the cytokine activity, we performed STAT3 luciferase reporter assay in mouse NIH3T3 cells, which respond to mOSM as expected (Supplementary Fig. 2b). These cells also respond to hOSM, albeit to a much less extent, confirming that hOSM can partially activate mouse receptors²⁷. Similar to hOSM, mOSM proteins derived from HEK293 (glycosylated) and *E. coli* (non-glycosylated), either in short form without the pro-domain (mOSM_short) or in long form with the pro-domain (mOSM_long), show largely similar activity

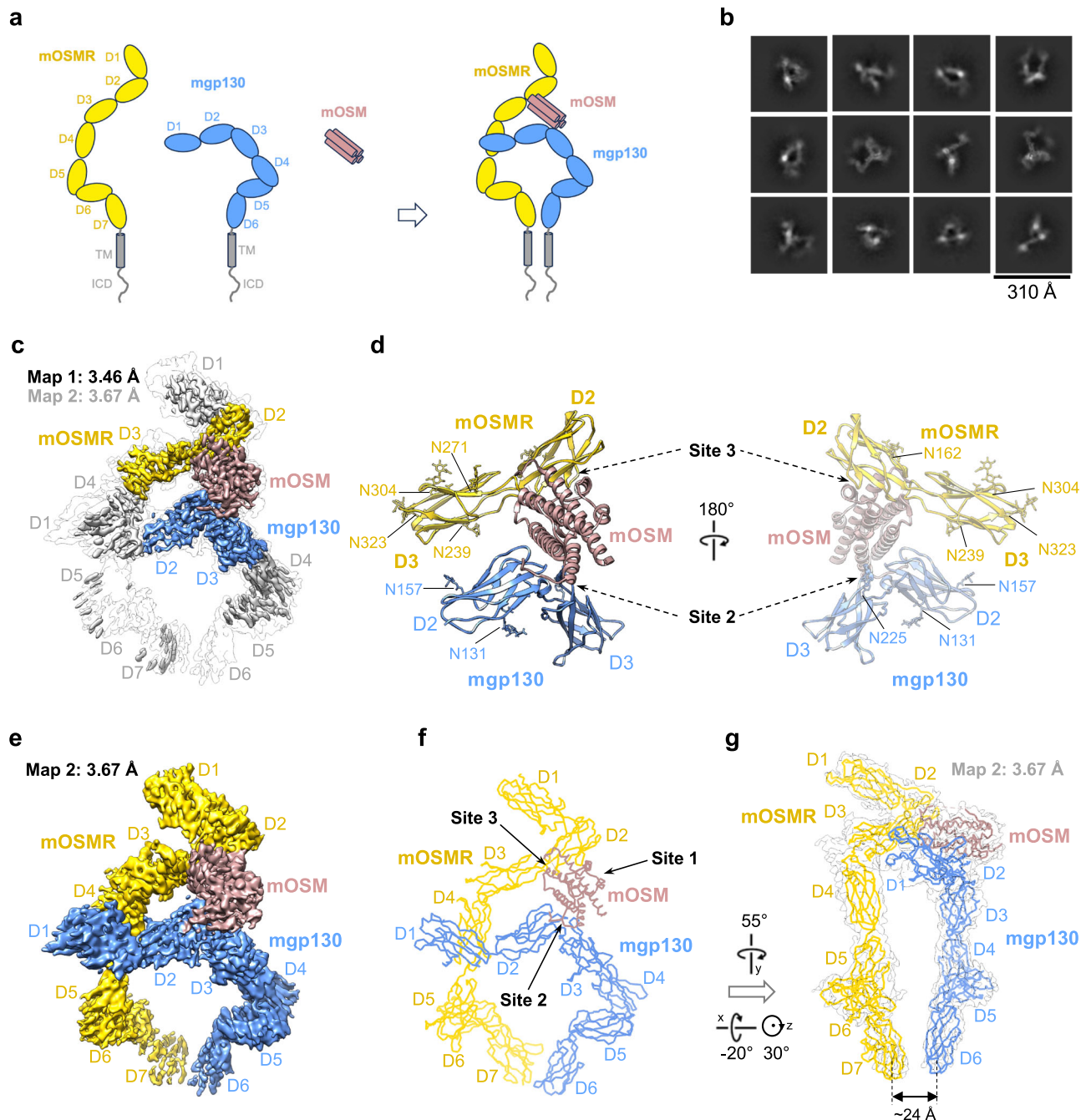


Fig. 4 | Cryo-EM structure of mouse type II OSM receptor complex (mOSM/mgp130/mOSMR complex). **a** Schematic representation of mouse OSM/gp130/OSMR complex assembly, with mOSMR, mgp130, and mOSM colored in gold, light blue, and brown, respectively. Transmembrane (TM) region and intracellular domains (ICD) of mOSMR and mgp130 were excluded from the constructs and were colored in gray. **b** Representative 2D class averages of mouse OSM/gp130/OSMR complex with full extracellular assembly. **c** 3.46 Å cryo-EM density map (Map 1) was overlaid with transparent Map 2 (3.67 Å). The assembly core regions of Map 1 (mOSM, mgp130 D2D3, and mOSMR D2D3) were colored as in (a) while the remaining parts of the map were colored in gray. **d** The atomic model of mouse

OSM/gp130/OSMR complex assembly core region (mOSM, mgp130 D2D3, and mOSMR D2D3) manually built and refined against Map 1 was shown in cartoon form in two orientations. Glycosylation sites in this region were highlighted in stick representation. **e** 3.67 Å cryo-EM density map (Map 2) of mouse OSM/gp130/OSMR complex colored as in (a). **f** Model of complete extracellular assembly of mouse OSM/gp130/OSMR complex depicted in C-alpha ribbon traces. **g** Side view of the full extracellular assembly model in transparent Map 2. Approximate distances between the bottom centers of mOSMR and mgp130 juxtamembrane domains is estimated.

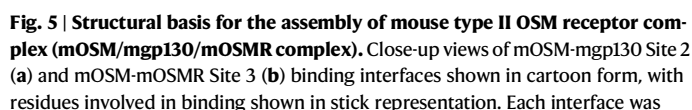
(Supplementary Fig. 3b), indicating that mOSM glycosylation and its pro-domain both do not obviously affect its activity.

In order to build a full model for the entire extracellular assembly of the mOSM/mgp130/mOSMR complex, the particles for generating Map 1 were further subjected to heterogeneous refinement to identify a subclass of particles with higher homogeneity at the receptor distal

domains (Supplementary Fig. 10a). Refinement of this subset of particles generated a new map (Map 2) with 3.67 Å global resolution (Supplementary Fig. 10a, f, g, Fig. 4e). The density of the distal domains in this second map is sufficient for placing AlphaFold models as rigid bodies to depict the overall architecture of the complex (Fig. 4f, g). As expected, an acute bend analogous to that seen in other signaling

aromatic anchor by packing against helix A via interactions with Q38, N41, Q42, and L45. In addition, as in the hOSM-hgp130 interface, L250 of mgp130 (equivalent to V252 of hgp130) serves as a supporting binding site from D3 through hydrophobic interactions with mOSM L45. On the ligand side, R26, Q38, and N135 are residues that contribute the three highest fractions of buried surface area. R26 in the N-terminal extension of mOSM makes extensive contacts with E163, E193, W195, and S209 of mgp130. Specifically, it forms a hydrogen bond with S209 and interacts with E193 via electrostatic interactions. Q38 in mOSM helix A is located in the center of the interface and is coordinated by Y189, V190, N191, and D213 of mgp130, with a hydrogen bond formed between mOSM Q38 and mgp130 D213. Lastly, N135 in the middle of mOSM helix C engages W146, A165, and V190 of mgp130 simultaneously, and pairs with mgp130 T166 through a hydrogen bond. Notably, the spatial cluster of hOSM residues (Q41, Q45, G145, N148, and N149) proved to be critical for hgp130 binding by mutagenesis^{17,37} are all conserved in mOSM (Supplementary Fig. 8). The corresponding mOSM residues (Q38, Q42, G132, N135, and N136,

Although mOSM only shares about ~45% sequence identity to hOSM (Supplementary Fig. 8), it engages mgp130 in an identical manner as how hOSM interacts with hgp130 at Site 2. The binding is also mediated by mOSM helices A and C with the N-terminal extension serving to stabilize the engagement (Fig. 5a). As in hOSM, the N-terminal extension of mOSM is tethered to helix C by the C28-C139 disulfide bond, leading to its rigid conformation. The middle portion of mOSM helix C (G132, N135, and N136) is captured by mgp130 W164 and V190. Y189 of mgp130, which is equivalent to F191 in hgp130, also functions as an



shown in two orientations. All-atom real-space refined model of the complex interaction core region shown in Fig. 4d was used for the analysis. Buried surface areas of the two binding interfaces were calculated by PDBBePISA.

respectively) also form a similar spatial cluster and interact with mgp130 in an analogous way (Supplementary Fig. 11). Moreover, hgp130 and mgp130 utilize a largely conserved/similar set of residues for binding to hOSM and mOSM, respectively (Supplementary Fig. 12). Notably, most of these hgp130 residues are also involved in hLIF binding in the human LIF signaling complex^{3,39}.

The architecture of mOSM-mOSMR Site 3 interface

Very broad contacts are made by 29 mOSM residues and 29 mOSMR residues at the Site 3 interface, which together bury a total surface area of 2,077 Å² (Fig. 5b). Not surprisingly, mOSM engages mOSMR mimicking the interactions between hOSM and hLIFR, with the conserved FXXK motif serving as a pivotal anchor point at the center of the binding interface. The aromatic ring of mOSM F170 at the N-terminal end of mOSM helix D also stacks against the peptide bond of a glycine residue (G225) in mOSMR and interacts with multiple surrounding residues, including N211, N213, I223, and V227, in a highly similar manner as how hOSM F185 engages hLIFR (Fig. 2b). Additionally, K173 in the FXXK motif of mOSM further strengthens the anchoring via hydrogen bond interactions with T208 and N211 of mOSMR. Consistently, alanine substitutions of the two equivalent residues in the FXXK motif of hOSM, F185 and K188, result in a great loss of hOSMR activation¹⁷. Analogous to the role of hOSM AB loop in engaging hLIFR, the AB loop of mOSM contributes a large fraction (41%) of buried surface area, indicating its critical role in mOSMR binding. As expected, alanine substitutions of five residues in the AB loop (Q60A/N61A/T64A/D66A/L67A, Supplementary Fig. 4e) dramatically decrease mOSM activity (Fig. 6a). In contrast, alanine substitutions of three BC loop residues (F114, L115, and K116) or two CD loop residues (D168 and V169) (Supplementary Fig. 4e), which are all contacting mOSMR, show no obvious effect on mOSM signaling, suggesting that these residues in the BC and CD loops are not major contributors for mOSMR binding. We also generated two other mOSM mutants, L115D and V169E (Supplementary Fig. 4e), hoping to introduce new electrostatic interactions or anion- π interactions to increase mOSM affinity to mOSMR and hence enhance its activity. However, none of the mutants shows improved activity (Fig. 6a).

The AB loop of mOSM primarily interacts with mOSMR through a network of hydrogen bond interactions mediated by N61, T64, and D66 (Fig. 5b). For example, N61 of mOSM forms hydrogen bonds with Q181, G209, and N211 of mOSMR and makes up the second largest buried surface area following F170 of mOSM. D66 in the short helix in mOSM AB loop is coordinated by mOSMR K179 via both hydrogen bond and salt bridge interactions, which appears to play a crucial role for the binding. As mentioned above, this aspartic acid residue is replaced by a lysine residue (K69) in hOSM (Supplementary Fig. 8), which might have eliminated the electrostatic interactions with mOSMR K179. Intriguingly, it has been shown that hOSM K69D mutant gained the ability to activate mOSMR²³, suggesting the critical role of this charged residue (mOSM D66, hOSM K69) in determining species-specific signaling.

On the mOSMR side, a few residues appear to be crucial for interacting with mOSM since they have quite large buried surface areas. N211 of mOSMR is located at the center of mOSM binding interface and makes extensive interactions with the AB loop and FXXK motif of mOSM (Fig. 5b). Four residues surrounding N211, including T208, N213, R222, and I223, engage mOSM AB loop and FXXK motif as well. The binding of mOSM to mOSMR is further stabilized by the N-terminal loop of mOSMR D3 packing against the posterior end of mOSM four-helix bundle. Notably, this loop is much longer compared with the loop in the corresponding domain of hLIFR (D4) (Supplementary Fig. 13). W264 of mOSMR in the middle of the loop is inserted into the cavity formed by helices A and D, as well as AB and BC loops (Fig. 5b, Supplementary Fig. 13). This single bulky residue contributes up to 156 Å² buried surface area by engaging a patch of residues

surrounding the cavity, including Q60, K113, F114, V169, T172, and K173. Based on the AlphaFold model, hOSMR also has a long D3 loop and a tryptophan residue (W267) in the loop that presumably can contribute to hOSM binding in a similar manner (Supplementary Fig. 13). Another two residues surrounding W264 of mOSMR, T263 and R265, also make quite broad contacts with the BC and CD loops of mOSM. Because of this long loop of mOSMR D3, the domain makes up 37% of the buried surface area from the receptor side. In contrast, the corresponding domain in hLIFR, D4, only contributes 8% and 14% of the buried surface area at the Site 3 interface for the binding of hOSM and hLIF, respectively. Notably, other than mOSMR W264, N211 of mOSMR is also conserved in hOSMR (N212), whereas the other six mOSMR residues mentioned above, including T208, N213, R222, I223, T263, and R265, are replaced by K209, Y214, G225, M226, G266, and S268 of hOSMR, respectively (Supplementary Fig. 14). To test whether mutating these hOSMR residues (alanine substitution for the two conserved residues: N211A, W267A; murinization for the non-conserved residues: K209T/Y214N, G225R/M226I, G266T/S268R) affect the receptor-mediated hOSM signaling, we performed STAT3 luciferase reporter assay in human Ramos.2G6.4C10 cells after stably overexpressing hOSMR WT or different mutants, which were confirmed to be localized on the cell surface at comparable expression levels (Supplementary Fig. 15). The cells could respond to hyper-hIL-6 (a fusion protein of human IL-6 and the soluble IL-6 receptor)⁴² but not hOSM (Supplementary Fig. 2c), indicating that there is endogenous hgp130 expression but no (or very low) hLIFR/hOSMR expression. Very robust STAT3 activation induced by hOSM is observed upon overexpression of exogenous WT hOSMR in the cells (Supplementary Fig. 2c). As expected, cells expressing hOSMR W267A or N212A mutant can only slightly respond or completely fail to respond to hOSM (Fig. 6b), confirming the crucial roles of these two residues in hOSM binding and signaling. Additionally, replacement of G266 and S268 in the long N-terminal loop of hOSMR D3 by corresponding mOSMR residues, T263 and R265, also greatly impairs hOSM signaling, suggesting that T263 and R265 of mOSMR might be two of the residues causing the non-responsiveness of mOSMR to hOSM²⁷. Intriguingly, the other two hOSMR murinization mutants, K209/Y214N and G266T/S268R, both show slightly improved capability to mediate hOSM signaling, indicating that the divergence of these four residues between hOSMR and mOSMR is not the reason why mOSMR does not respond to hOSM.

Discussion

Nearly four decades after the discovery of OSM, we here report the structural basis for the complete extracellular assembly of both type I and type II OSM receptor complexes, elucidating similarities and divergences of these two complexes and other receptor complex of this family such as the LIF signaling complex.

OSM and LIF are two IL-6 family members that do not require an alpha receptor for signaling. Therefore, Site 1 of both cytokines are left empty in their signaling complexes. Our previous study suggested that the N-terminal extension of LIF preceding helix A adopts a rigid conformation by tethering to helix C through two disulfide bonds (C34-C156 and C40-C153) and introduces additional contacts with gp130 at Site 2, which might serve to improve the binding affinity and stabilize the complex assembly³. Similarly, our current study demonstrates that both hOSM and mOSM have a rigid N-terminal extension tethered to helix C by a disulfide bond that results in increased buried surface area at the Site 2 binding interface. Through site-directed mutagenesis, we show that either disruption of the rigidity or truncation of hOSM N-terminal extension would reduce its binding affinity to hgp130 and attenuate the signaling at low ligand concentration. However, when hOSM reaches higher concentration, the contribution of the rigid N-terminal extension appears to be less significant, indicating that the N-terminal extension is not a crucial determinant that leads to the

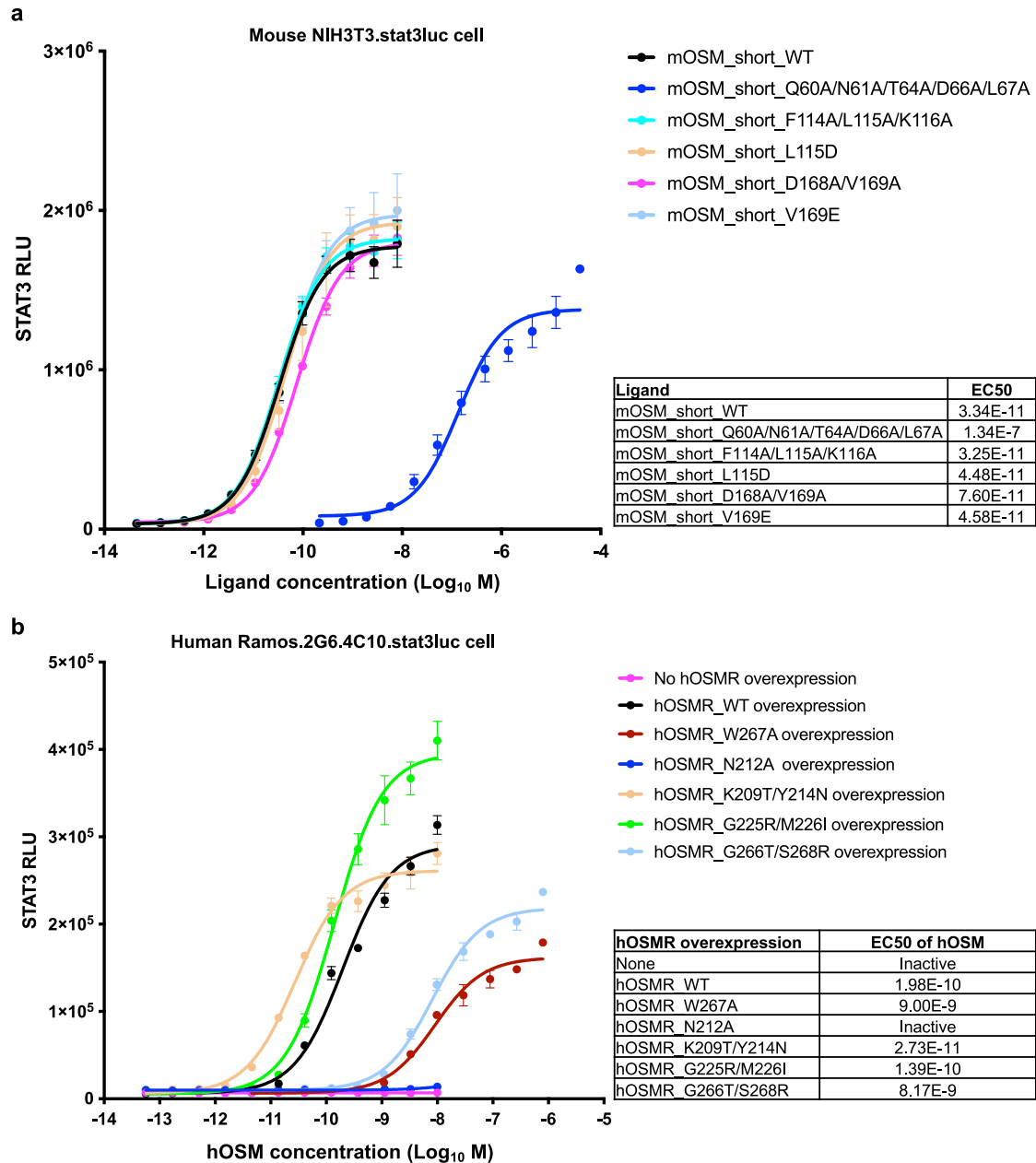


Fig. 6 | Structure based mutagenesis studies identified an antagonistic mOSM mutant and key hOSMR residues involved in hOSM binding and signaling. **a** STAT3-luciferase reporter assay was performed in mouse NIH3T3 cells after treating the cells with short form mOSM WT and five mutant proteins with mutations at Site 3. The data shown are representative of 3 independent experiments with similar results. Error bars represent standard deviations. RLU: relative

luminescence units. **b** WT hOSMR or six hOSMR mutants were stably over-expressed in human Ramos.2G6.4C10.stat3luc cells; STAT3-luciferase reporter assay was performed after treating the cells with *E.coli*-derived short form hOSM protein (R&D, #295-OM). The data shown are representative of 3 independent experiments with similar results. Error bars represent standard deviations. Source data are provided as a Source Data file.

alpha receptor independence of hOSM. Instead, it acts more like a contributor that enhances its affinity to hgp130 and boosts the signaling at relatively low cytokine concentration. Compared with free hOSM, the N-terminal extension of hOSM in the type I receptor complex adopts a different conformation upon binding to hgp130, while there is no major conformational change for the rest of the cytokine (Supplementary Fig. 16). Notably, the buried surface areas between gp130 and the cytokine at Site 2 in hOSM type I receptor complex, mOSM type II receptor complex, and LIF receptor complex³ are 1,513 Å², 1,437 Å², 1,412 Å², respectively, which are all much broader than the buried surface areas of the cytokine-gp130 interface in hCNTF receptor complex (1,141 Å²) and hCLCF1 receptor complex (942 Å²)³.

This might be the reason why hCNTF and hCLCF1 require the alpha receptor CNTFRα to stabilize the cytokine binding to gp130 at Site 2, while hOSM/mOSM and hLIF do not need an alpha receptor for the signaling complex assembly.

It has been shown that Site 3 of hLIF represents a higher affinity binding site in the hLIF signaling complex, whereas in both type I and type II hOSM receptor complexes the higher affinity site is Site 2, leading to different assembly order of each complex^{9,13,20}. In support of this, a hLIF-hLIFR assembly intermediate was observed in our previous characterization of hLIF signaling complex³, while a hOSM-hgp130 subcomplex was present in the current hOSM type I receptor complex sample (Supplementary Fig. 1b). A major difference between

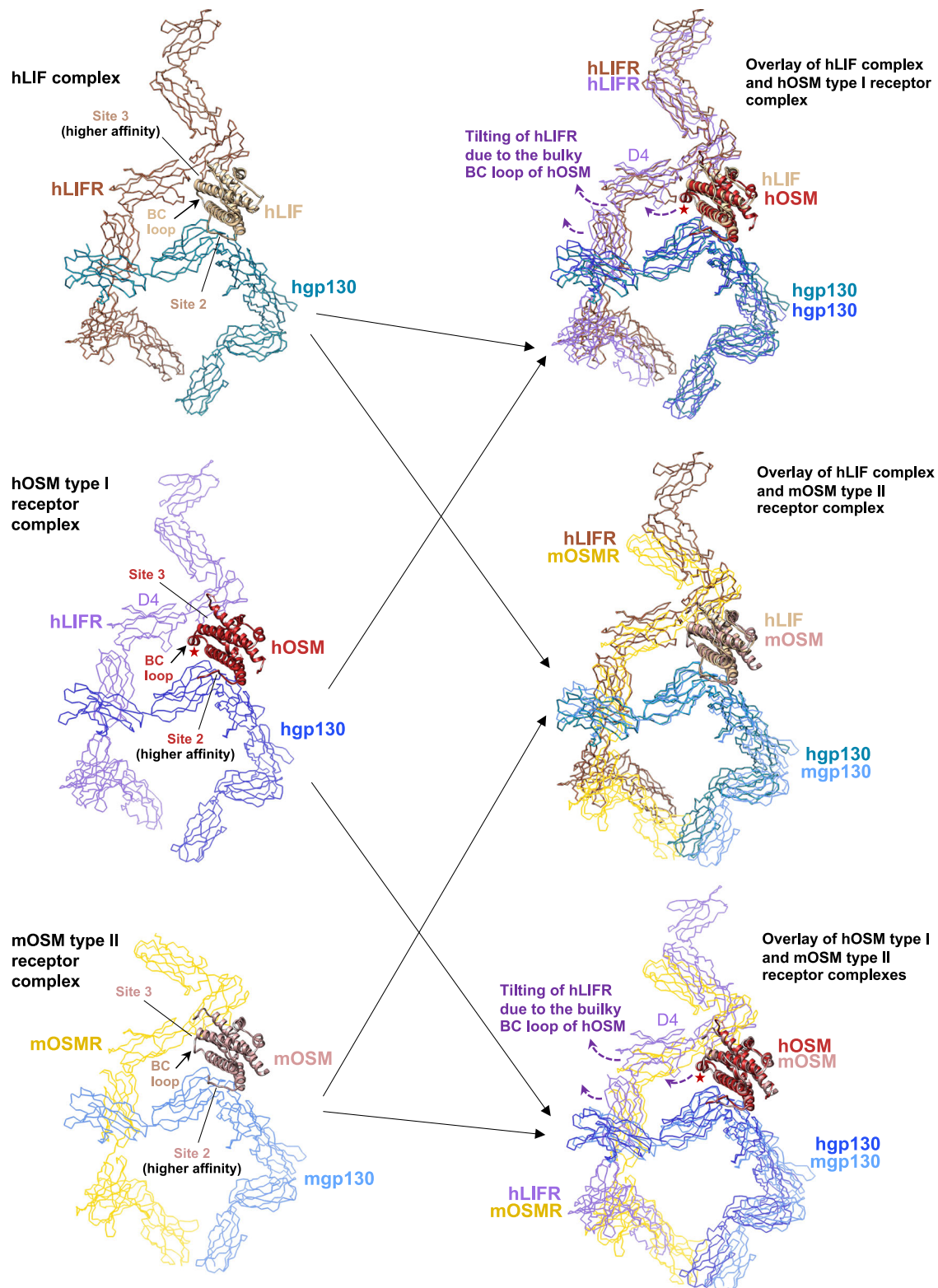


Fig. 7 | Structural comparison of hLIF complex, hOSM type I and mOSM type II receptor complexes. Structures of hLIF signaling complex, hOSM type I and mOSM type II receptor complexes were aligned on the cytokines to the same

orientation (left) and superimposed onto each other (right). The unique helical BC loop of hOSM was annotated with a red star. The cytokines were shown in cartoon form while the receptors were depicted in C-alpha ribbon traces.

structures of hOSM and hLIF is that hOSM possesses a longer BC loop that contains a short helix (Supplementary Fig. 16). Intriguingly, hOSM variants with shortened BC loop show higher affinity toward hLIFR than toward hgp130¹³, suggesting that the bulky BC loop in WT hOSM may alter the way hOSM engages hLIFR at Site 3. Our structural data

show that in the hOSM type I complex, the helical BC loop of hOSM pushes hLIFR D4 away from the cytokine (Fig. 7), leading to a tilted binding angle of hLIFR relative to the angle of hLIFR binding to Site 3 of hLIF (Supplementary Fig. 13). This forced tilting of hLIFR by the bulky hOSM BC loop may have reduced the Site 3 binding affinity through

modulation of interactions. Based on the homology modeling of human OSM type II receptor complex, hOSMR would also adopt a similar angle as hLIFR upon binding to hOSM to avoid clashing with the BC loop (Supplementary Fig. 13). In contrast, hgp130 adopts a very similar binding mode to both hOSM and hLIF at Site 2 (Fig. 7). Interestingly, the size of mOSM BC loop is similar to that of hLIF (Supplementary Fig. 16), which allows mOSMR binding to mOSM with a similar angle as that between hLIF and hLIFR (Fig. 7, Supplementary Fig. 13). However, mOSM still appears to show higher affinity toward mgp130 than toward mOSMR since a mOSM-mgp130 assembly intermediate was observed (Supplementary Fig. 10b). Besides the BC loop, the AB loop and the N-terminus of helix D constitute the rest of the Site 3 binding site in this family of cytokines. Intriguingly, substitution of the hOSM AB loop with that of hLIF eliminated its ability to activate hOSMR while replacement of hLIF AB loop and D-helix with hOSM counterparts was sufficient for hOSMR activation²⁸, suggesting that the AB loop of OSM renders this cytokine a unique ability to bind and activate OSMR. Indeed, we observed quite different conformations of the AB loops of hOSM and mOSM compared with that of hLIF (Supplementary Fig. 16).

Through structure-based protein engineering, we identified multiple hOSM mutations that can greatly reduce or totally abolish the cytokine activity, such as Q41R, Q41W/Q45W, N148R, and N148W at Site 2, and V67A/K69A/L70A/H73A at Site 3. Some of these antagonistic mutants may have therapeutic value for treating diseases with elevated hOSM signaling. Alanine substitutions of five residues in the AB loop of mOSM Site 3 (Q60A/N61A/T64A/D66A/L67A) substantially decrease mOSM activity. We also attempted to identify agonistic mutants of hOSM and mOSM but did not succeed. In addition, alanine substitution of two hOSMR residues, N212 in D2 and W267 in D3, which are both conserved in mOSMR, completely eliminate and largely reduces the receptor's responsiveness to hOSM, respectively, indicating that these two hOSMR residues are critical for hOSM binding. Moreover, mutation of two residues in the long N-terminal loop of hOSMR D3, G266 and S268, to corresponding mOSMR residues, also dramatically decreases hOSMR response to hOSM, suggesting that the divergence of these two residues between mOSMR and hOSMR is largely responsible for the lack of mOSMR activation by hOSM. In murine cells, mOSM mainly signals via mgp130 and mOSMR heterodimerization because mOSM has much lower binding affinity to mLIFR than to mOSMR^{23–26}. Our structural data demonstrate that the long N-terminal loop of mOSMR D3 makes extensive interactions with mOSM. In contrast, mLIFR has a much shorter loop at a similar location in D4 that appears to contribute significantly less to mOSM binding. The obvious difference in the length of this loop between mLIFR and mOSMR may explain why mOSM binds to mOSMR with a much higher affinity compared with its affinity towards mLIFR. Furthermore, we confirmed that the glycosylation and the C-terminal pro-domain of hOSM and mOSM both do not obviously affect the cytokine activity in vitro, although hOSM pro-domain has been implicated in hOSM binding to extracellular matrix, which may prolong hOSM signaling in vivo¹¹.

We previously showed that the IL-6 family cytokine signaling receptors, including gp130, LIFR, and IL-27R α , all have an $\sim 80^\circ$ acute bend between the third to the last and the second to the last extracellular domains (gp130 D4D5, LIFR D6D7, IL-27R α D3D4)³. This bent receptor conformation appears to be a crucial geometry for signaling since the bends of both signaling receptors towards each other could serve to bring the bottom centers of the receptor juxtamembrane domains to close proximity (usually less than 30 Å), which allows dimerization and trans-phosphorylation of Janus kinases (JAKs) bound to the intracellular domains of the two receptors^{40,43}. Consistently, our data here suggest that both hOSM type I complex and mOSM type II complex have a juxtamembrane distance of ~ 25 Å. As expected, a similar acute bend was also observed between D5 and D6 of mOSMR,

further confirming that the bent conformation is a common feature for this family of receptors. It has been shown that two hgp130 residues, W333 in D4 and W470 in D5, are buried in the center of hgp130 D4D5 interface by packing against opposing domains through extensive hydrophobic interactions and play critical roles in maintaining the bent configuration of the two domains². Notably, these two tryptophan residues, as well as a lysine residue (K352) that is also involved in the bending, are completely conserved across this family of receptors, including hgp130, mgp130, mOSMR, hLIFR, and hIL-27R α ² (Supplementary Fig. 17). Additionally, deletion of gp130 membrane-proximal domains has been shown to impair IL-6, IL-11, LIF, and OSM signaling^{44,45}, likely because the deletions have either disrupted the bent conformation of gp130 or altered the relative positions of the receptor juxtamembrane domains and thus placed the two receptor TM helices of the signaling complex in a geometry that is not favorable for the activation of downstream signaling. Corroborating this notion, changes in angle/distance between cytokine receptor juxtamembrane domains have been shown to lead to different signaling outputs⁴⁶.

Together, our structures of the full extracellular assemblies for both type I and type II OSM receptor complexes reveal the structural basis for complex formation. The detailed protein-protein interactions and critical contacting residues revealed by cryo-EM structures and mutagenesis studies may provide valuable guidance for developing therapeutic treatments for diseases arising from disorders in OSM signaling.

Methods

Protein purification

The signal peptides were counted in the numbering of residues for all proteins mentioned in this paper. hgp130 ectodomain (aa E23–E619), hLIFR ectodomain (aa Q45–S833), and mgp130 ectodomain (aa Q23–E617) used for OSM signaling complexes formation were all C-terminal myc-myc-His (mmH)-tagged secreted proteins expressed in Chinese Hamster Ovary (CHO-K1) cells. hOSM/mOSM wild-type (WT) proteins and mutants used in the bioassays were C-terminal mmH tagged secreted proteins expressed in HEK-293 (Expi293F) cells. WT hOSM were expressed and purified in both long form with the pro-domain (hOSM_long, aa A26–R252) and short form without the pro-domain (hOSM_short, aa A26–R221). All hOSM mutants were short form proteins (hOSM_short, aa A26–R221; for mutant Δ (A26–E34)/C152S: aa Y35–R221). WT mOSM and five mOSM mutants were all in short form (mOSM_short, aa A24–R206). To purify these proteins from the medium, filtered cell culture supernatants were buffer exchanged through dialysis against DPBS and loaded onto pre-equilibrated Talon columns (Clontech, #635682). After washing the columns with DPBS containing 500 mM NaCl, followed by a second wash with DPBS plus 500 mM NaCl and 5 mM Imidazole, the proteins were eluted with DPBS plus 500 mM NaCl and 200 mM Imidazole. Human gp130 (aa E23–E619) used in the Biacore study has a hFc tag and was purified with a MabSelect SuRe (Cytiva) column, followed by elution with 100 mM glycine pH 2.7. The eluates were dialyzed against DPBS with 5% glycerol, and subsequently, the proteins were further purified by size exclusion chromatography (SEC), concentrated, and frozen for future use.

Full length hgp130 with a C-terminal Flag tag was expressed in FreeStyle™ 293-F Cells (Thermo Fisher, #R79007) after transfection with Lipofectamine 2000 (Thermo Fisher, #11668027). Cells pellet was mixed with solubilization buffer (20 mM HEPES pH 7.4, 150 mM NaCl, 1% Lauryl Maltose Neopentyl Glycol (LMNG, Anatrace, #NG310), cOmplete EDTA-free protease inhibitors) and rotated at 4°C for 1 hr. After centrifugation, the supernatant was incubated with anti-Flag M2 affinity gel (Sigma Aldrich, #A2220). After washing with SEC buffer (20 mM HEPES pH 7.4, 150 mM NaCl, 0.01% LMNG), the protein was eluted with SEC buffer containing 0.15 mg/ml of 3X Flag peptide and further purified by SEC. The protein was concentrated with a 100-kDa

molecular weight cutoff (MWCO) centrifugal concentrator and flash-frozen in liquid nitrogen for future use.

The Fab fragment of the anti-gp130 antibody B-S12 (Abcam, #ab27359) was generated using Pierce™ Mouse IgG1 Fab and F(ab')₂ Preparation Kit (Thermo Fisher, #44980) following the manufacturer's instructions.

Three proteins used in structural studies were purchased from commercial sources, including *E. coli*-derived mOSM protein in short form (aa A24-R206, R&D Systems #495-MO), HEK293-derived hOSM protein in short form (aa A26-R221, R&D Systems #8475-OM), and HEK293-derived mOSMR protein (aa E24-L738, SinoBiological #50500-M08H). Other hOSM and mOSM proteins used in the bioassays include hOSM_short (*E. coli*, aa A26-R221, R&D #295-OM), mOSM_short (HEK293, aa A24-R206, Sino #50112-M08H), mOSM_long (HEK293, aa N25-R263, Abcam #ab280335), and mOSM_long (*E. coli*, aa A24-R206, Sino #50112-MNAE).

Complex preparation

Human type I OSM receptor complex was reconstituted by mixing hgp130 ectodomain, hLIFR ectodomain, and HEK293-derived short form hOSM protein (aa A26-R221) at an equal molar ratio followed by incubation at 4 °C for 1 h. The complex was further purified over a Superdex 200 increase 10/300 GL gel filtration column equilibrated with 50 mM Tris pH 7.5, 150 mM NaCl. Peak fractions containing the target complex were collected and concentrated to ~2.8 mg/ml using a 30 kDa MWCO centrifugal concentrator. Mouse type II OSM receptor complex was reconstituted by mixing mgp130 ectodomain, mOSMR ectodomain, and *E. coli*-derived short form mOSM protein (aa A24-R206) at an equal molar ratio followed by incubation at 4 °C for 1 h. The mixture was concentrated to ~2.8 mg/ml using a 30 kDa MWCO centrifugal concentrator. Full length hgp130 protein (~0.5 mg/ml) solubilized in detergent was mixed with the anti-gp130 antibody B-S12 Fab (~3 mg/ml) at an equal molar ratio followed by incubation at 4 °C for 30 min.

Cryo-EM sample preparation and data collection

The hOSM type I receptor complex or mOSM type II receptor complex was mixed with ~0.15% Amphipol PMAL-C8 (Anatrace) immediately before pipetting 3.5 µL of the mixture onto a UltrAufoil R1.2/L1.3, 300 mesh grid (Quantifoil), while 3.5 µL of the full length hgp130/B-S12 Fab complex was directly applied to the grid. The grid was blotted for 4.5 s at a force of 0 and plunge frozen into liquid ethane using a Vitrobot Mark IV (ThermoFisher) operated at 4 °C and 100% humidity. The hOSM type I receptor complex and mOSM type II receptor complex grids were then loaded into a Titan Krios G3i microscope (ThermoFisher) equipped with a K3 camera and energy filter (Gatan) for data collection at a nominal magnification of 105 kx (0.86 Å/pixel). Cryo-EM data for the full length hgp130/B-S12 Fab complex was collected in a Glacios microscope equipped with a Falcon 4i camera and energy filter at a magnification of 165 kx (0.696 Å/pixel). Automated data collections were carried using EPU v2.12 (ThermoFisher) with a defocus range of ~1.4 to ~2.6 µm.

Cryo-EM data processing

Cryo-EM data were processed using cryoSPARC v2⁴⁷. Movies were motion corrected by Patch motion correction and CTF parameters were estimated by Patch CTF estimation. Particles were initially picked using Blob picker from ~500 micrographs to generate 2D class averages to be used as templates for the subsequent template picking. Junk particles were removed by multiple rounds of 2D classification, followed by Ab initio reconstruction, Homogeneous refinement, and Heterogeneous refinement to identify the best class of particles representing the target protein complex. These particles were further refined using non-uniform refinement⁴⁸ to generate the final cryo-EM

density map. Cryo-EM data processing statistics were summarized in Supplementary Table 1.

For the hOSM type I receptor complex, 10,428,767 particles were picked by template picking (Supplementary Fig. 1). 360,997 particles were left after 2D classification, which were subjected to Ab initio reconstruction to isolate a class of 219,837 'good' particles. Non-uniform refinement of these particles led to a 3.59 Å map (Map 1) which has well resolved interaction core region but fragmented hLIFR D6-D8 density. This map was used for manual model building and all-atom real-space refinement of the assembly core region (hOSM, hgp130 D2D3, and hLIFR D3D4). These particles were further subjected to heterogeneous refinement, generating two classes with poorly resolved hLIFR D6-D8, which have 74,713 particles and 73,610 particles, respectively. The third class of 71,514 particles show much stronger hLIFR D6-D8 density. Non-uniform refinement of the third class yielded another map (Map 2) with lower global resolution (3.99 Å) but improved hLIFR D6-D8 density. This map was used to generate a complete model for the full extracellular portion of the hOSM type I receptor complex.

For the mOSM type II receptor complex, 10,449,418 particles were picked by template picking (Supplementary Fig. 10). 1,261,689 particles were left after 2D classification, which were subjected to Ab initio reconstruction to isolate a class of 270,829 'good' particles. Non-uniform refinement of these particles led to a 3.46 Å map (Map 1) which has well resolved interaction core region but fragmented mOSMR D5-D7 density. This map was used for manual model building and all-atom real-space refinement of the assembly core region (mOSM, mgp130 D2D3, and mOSMR D2D3). These particles were further subjected to heterogeneous refinement, generating two classes with poorly resolved mOSMR D5-D7, which have 98,225 particles and 73,016 particles, respectively. The third class of 99,588 particles show much better mOSMR D5-D7 density. Non-uniform refinement of the third class yielded another map (Map 2) with lower global resolution (3.67 Å) but improved mOSMR D5-D7 density. This map was used to generate a complete model for the full extracellular portion of the mOSM type II receptor complex.

For the full length hgp130/B-S12 Fab complex, 2,478,065 particles were picked by template picking. 165,090 particles were left after 2D classification, which were subjected to Ab initio reconstruction to isolate a class of 45,829 'good' particles. Non-uniform refinement of these particles led to a 4.40 Å map (Supplementary Fig. 5c).

Model building and refinement

AlphaFold models of hOSM, hgp130, hLIFR, mOSM, mgp130, and mOSMR were used as initial models for model building. A combination of picked initial models (or selected domains of these models) was docked into corresponding cryo-EM density map using Fit-in-map of UCSF Chimera 1.16⁴⁹. For both hOSM type I and mOSM type II receptor complexes, only the well resolved regions around the assembly core of each complex (hOSM, hgp130 D2D3, and hLIFR D3D4 of the hOSM type I receptor complex; mOSM, mgp130 D2D3, and mOSMR D2D3 of the mOSM type II receptor complex) were manually modeled in Coot 0.8.9⁵⁰ and real-space refined with secondary structure and non-crystallographic symmetry (NCS) restraints in Phenix 1.19⁵¹. The geometries of the structures were validated by using MolProbity⁵² in Phenix and the statistics were summarized in Supplementary Table 1. These two structures were further subjected to PDBePISA analysis⁵³ to identify residue-residue interactions (shown in Figs. 2, 5) and calculate buried surface areas of individual residues or all residues at each binding interface.

Complete models containing full extracellular assemblies of hOSM type I and mOSM type II receptor complexes were also generated by combining the abovementioned structures of the assembly core regions and models of the receptor distal domains derived from

AlphaFold models. Briefly, the models of the receptor distal domains were docked into the corresponding density with the guidance of available receptor structures/AlphaFold models using the Fit-in-map function of Chimera, followed by connection of these models to the structures of the complex interaction core region in Coot. The composite models with full ECDs were further real-space refined against corresponding cryo-EM maps using the rigid-body strategy in Phenix. These models containing rigid-body fitted receptor distal domains were used to present the overall architectures of the extracellular portions of these complexes and relative positions of the membrane-proximal domains (shown in Figs. 1, 4). The structure refinement statistics were summarized in Supplementary Table 1.

STAT3 luciferase assay

Three STAT3 luciferase reporter cell lines were generated by transducing a lentivirus encoding a STAT3-luciferase (stat3luc) reporter (Qiagen, #CLS-6028L) into human IMR-32 cells (ATCC, #CCL-127) and mouse NIH3T3 cells (ATCC, #CRL-1658), or another stat3luc reporter (SA bioscience, #CLS-6028L) into human Ramos.2G6.4C10 cells (ATCC, #CRL-1923). hOSMR WT or indicated mutant was stably overexpressed in Ramos.2G6.4C10.stat3luc cells through lentivirus transduction and Blasticidin selection. Human IMR32.stat3luc cells and mouse NIH3T3.stat3luc cells were plated overnight in assay buffer containing OptiMEM (Thermo Fisher, #51985), 1% Bovine Serum Albumin (Sigma, #A7030), and 0.1% Fetal Bovine Serum (FBS) (Seradigm, #97068-085), in white PDL-coated 384 well or 96 well plates (Corning, #354660 or #354651). The next day, cells were treated with indicated cytokines titrated in 1:3 dilution series for 6 hrs. Human Ramos.2G6.4C10.stat3luc cells with or without overexpression of hOSMR WT or indicated hOSMR mutants were plated in growth media RPMI1640 (Thermo Fisher, #11875135) with 10% FBS and 1x Penicillin-Streptomycin-Glutamine (Thermo Fisher, #10378016). One hour after plating, cells were treated with *E.coli*-derived short form hOSM protein (R&D, #295-OM) titrated in 1:3 dilution series overnight. To measure luciferase activity, an equal volume of OneGlo (Promega, #E6130) was added to each well, followed by placement of a white adhesive bottom seal (PerkinElmer/Revvity, #6005199) on the bottom of each plate. The plate was shaken for 5 min and read for luminescence on the PerkinElmer Envision plate reader (PerkinElmer, #2105). The data were analyzed in GraphPad Prism. Each experiment was repeated 2 to 5 times with similar trends observed. The data from a representative experiment were shown.

hOSMR WT and mutant lentivirus packing and transduction

To pack the lentivirus, each lentiviral construct containing a hOSMR WT or mutant gene and a Blasticidin selection marker was mixed with the Lenti-X HTX Packaging Mix (Clontech, #631248) and transfected into HEK293T/17 cells (ATCC, #CRL-11268) using FuGENE® HD Transfection Reagent (Promega, #E2311). Viral particles were harvested 48 h post-transfection, filtered using a 0.45 µm syringe filter, and concentrated using a 30 kDa MWCO centrifugal concentrator. To transduce Ramos.2G6.4C10.stat3luc cells, 2.5×10^5 cells were seeded in 1 mL of each lentivirus sample in the presence of 5 µg/ml Polybrene (Millipore, TR-1003-G). The media was replaced with fresh media 24 hrs after transduction. A day later, the media was further changed to selection media containing 10 µg/ml Blasticidin. Two weeks after selection, the cells were stained with an isotype control antibody or an anti-hOSMR antibody conjugated with APC (Thermo Fisher, #MA5-46728), followed by flow cytometry analysis to examine the expression and cell surface localization of hOSMR WT and mutant proteins.

Flow cytometry

100,000 human Ramos.2G6.4C10.stat3luc cells with or without overexpression of hOSMR WT and indicated mutants were collected and washed with PBS with 1% BSA at 4 °C. Cells were stained with an isotype

antibody control (Alexa Fluor 647-conjugated goat anti-rabbit antibody, Jackson, #111-605-003) or an APC-conjugated anti-hOSMR antibody (Thermo Fisher, #MA5-46728) for 30 min on ice, protected from light. After staining, cells were washed 3 times with ice cold PBS with 1% BSA and analyzed on CytoFlex S (Beckman Coulter). Flow cytometry data were acquired using CytExpert 2.4 and analyzed using FlowJO 10.8.0.

Surface plasmon resonance

The kinetics of hOSM proteins binding to hgp130.hFc were determined on a Biacore T200 biosensor (Cytiva), using a Series S CM5 sensor chip in filtered and degassed HBS-EP running buffer (10 mM HEPES, 150 mM NaCl, 3 mM EDTA, 0.05% (v/v) polysorbate 20, pH 7.4) at 37 °C. The CM5 sensor chip was immobilized with mouse anti-hFc mAb (REGN2567) using standard amine-coupling chemistry⁵⁴. hgp130.hFc was captured by an anti-hFc antibody immobilized on the chip surface via amine coupling (Cytiva, #BR-1000-50), and varying concentration of hOSM proteins were injected followed by a dissociation phase. At the end of each cycle, anti-hFc-captured hgp130.hFc were removed using 12-second injection of 20 mmol/L phosphoric acid. All of the specific SPR binding sensorgrams were double-reference subtracted as reported previously⁵⁵ and the kinetic parameters were obtained by globally fitting the double-reference subtracted data to a 1:1 binding model with mass transport limitation using the Scrubber 2.0c curve-fitting software (BioLogic Software). The dissociation rate constant (kd) was determined by fitting the change in the binding response during the dissociation phase and the association rate constant (ka) was determined by globally fitting analyte binding at different concentrations. The equilibrium dissociation constant (KD) was calculated from the ratio of the kd and ka.

Reporting summary

Further information on research design is available in the Nature Portfolio Reporting Summary linked to this article.

Data availability

The cryo-EM density maps and accompanying atomic coordinates have been deposited to Electron Microscopy Data Bank (EMDB) and Protein Data Bank (PDB) with the following accession codes: type I hOSM receptor complex (hOSM/hgp130/hLIFR complex) Map 1 and model for assembly core region (EMD-42903 [<https://www.ebi.ac.uk/pdbe/entry/emdb/EMD42903>] and 8V2A), type I hOSM receptor complex Map 2 and model for full extracellular assembly (EMD-42902 [<https://www.ebi.ac.uk/pdbe/entry/emdb/EMD42902>] and 8V29), type II mOSM receptor complex (mOSM/mgp130/mOSMR complex) Map 1 and model for assembly core region (EMD-42905 [<https://www.ebi.ac.uk/pdbe/entry/emdb/EMD42905>] and 8V2C), type II mOSM receptor complex Map 2 and model for full extracellular assembly (EMD42904 [<https://www.ebi.ac.uk/pdbe/entry/emdb/EMD42904>] and 8V2B). Source data are provided with this paper. Regeneron materials described in this manuscript may be made available to qualified, academic, noncommercial researchers through a materials transfer agreement upon request at https://regeneron.envisionpharma.com/vt_regeneron/. For questions about how Regeneron shares materials, use the email address pre-clinical.collaborations@regeneron.com. Source data are provided with this paper.

References

- Kang, S., Narazaki, M., Metwally, H. & Kishimoto, T. Historical overview of the interleukin-6 family cytokine. *J. Exp. Med.* **217**(2020).
- Xu, Y. et al. Crystal structure of the entire ectodomain of gp130: insights into the molecular assembly of the tall cytokine receptor complexes. *J. Biol. Chem.* **285**, 21214–21218 (2010).

3. Zhou, Y. et al. Structural insights into the assembly of gp130 family cytokine signaling complexes. *Sci. Adv.* **9**, eade4395 (2023).
4. Stahl, N. et al. Association and activation of Jak-Tyk kinases by CNTF-LIF-OSM-IL-6 beta receptor components. *Science* **263**, 92–95 (1994).
5. Stahl, N. et al. Choice of STATs and other substrates specified by modular tyrosine-based motifs in cytokine receptors. *Science* **267**, 1349–1353 (1995).
6. Darnell, J. E. Jr., Kerr, I. M. & Stark, G. R. Jak-STAT pathways and transcriptional activation in response to IFNs and other extracellular signaling proteins. *Science* **264**, 1415–1421 (1994).
7. Luttkien, C. et al. Association of transcription factor APRF and protein kinase Jak1 with the interleukin-6 signal transducer gp130. *Science* **263**, 89–92 (1994).
8. Dey, G. et al. Signaling network of Oncostatin M pathway. *J. Cell Commun. Signal* **7**, 103–108 (2013).
9. Mosley, B. et al. Dual oncostatin M (OSM) receptors. Cloning and characterization of an alternative signaling subunit conferring OSM-specific receptor activation. *J. Biol. Chem.* **271**, 32635–32643 (1996).
10. Wolf, C. L., Pruett, C., Lighter, D. & Jorcyk, C. L. The clinical relevance of OSM in inflammatory diseases: a comprehensive review. *Front Immunol.* **14**, 1239732 (2023).
11. Ryan, R. E. et al. Oncostatin M binds to extracellular matrix in a bioactive conformation: implications for inflammation and metastasis. *Cytokine* **72**, 71–85 (2015).
12. Hermanns, H. M. Oncostatin M and interleukin-31: Cytokines, receptors, signal transduction and physiology. *Cytokine Growth Factor Rev.* **26**, 545–558 (2015).
13. Chollangi, S., Mather, T., Rodgers, K. K. & Ash, J. D. A unique loop structure in oncostatin M determines binding affinity toward oncostatin M receptor and leukemia inhibitory factor receptor. *J. Biol. Chem.* **287**, 32848–32859 (2012).
14. Tseng, P. Y. & Hoon, M. A. Oncostatin M can sensitize sensory neurons in inflammatory pruritus. *Sci. Transl. Med.* **13**, eabe3037 (2021).
15. Lee, B. Y. et al. Heterocellular OSM-OSMR signalling reprograms fibroblasts to promote pancreatic cancer growth and metastasis. *Nat. Commun.* **12**, 7336 (2021).
16. Rose, T. M. et al. The genes for oncostatin M (OSM) and leukemia inhibitory factor (LIF) are tightly linked on human chromosome 22. *Genomics* **17**, 136–140 (1993).
17. Deller, M. C. et al. Crystal structure and functional dissection of the cytostatic cytokine oncostatin M. *Structure* **8**, 863–874 (2000).
18. Jeffery, E., Price, V. & Gearing, D. P. Close proximity of the genes for leukemia inhibitory factor and oncostatin M. *Cytokine* **5**, 107–111 (1993).
19. Giovannini, M., Djabali, M., McElligott, D., Sella, L. & Evans, G. A. Tandem linkage of genes coding for leukemia inhibitory factor (LIF) and oncostatin M (OSM) on human chromosome 22. *Cytogenet Cell Genet* **64**, 240–244 (1993).
20. Gearing, D. P. et al. The IL-6 signal transducer, gp130: an oncostatin M receptor and affinity converter for the LIF receptor. *Science* **255**, 1434–1437 (1992).
21. Auguste, P. et al. Signaling of type II oncostatin M receptor. *J. Biol. Chem.* **272**, 15760–15764 (1997).
22. Drechsler, J., Grotzinger, J. & Hermanns, H. M. Characterization of the rat oncostatin M receptor complex which resembles the human, but differs from the murine cytokine receptor. *PLoS One* **7**, e43155 (2012).
23. Adrian-Segarra, J. M. et al. The AB loop of oncostatin M (OSM) determines species-specific signaling in humans and mice. *J. Biol. Chem.* **293**, 20181–20199 (2018).
24. Walker, E. C. et al. Murine Oncostatin M Acts via Leukemia Inhibitory Factor Receptor to Phosphorylate Signal Transducer and Activator of Transcription 3 (STAT3) but Not STAT1, an Effect That Protects Bone Mass. *J. Biol. Chem.* **291**, 21703–21716 (2016).
25. Walker, E. C. et al. Oncostatin M promotes bone formation independently of resorption when signaling through leukemia inhibitory factor receptor in mice. *J. Clin. Invest.* **120**, 582–592 (2010).
26. Ichihara, M., Hara, T., Kim, H., Murate, T. & Miyajima, A. Oncostatin M and leukemia inhibitory factor do not use the same functional receptor in mice. *Blood* **90**, 165–173 (1997).
27. Lindberg, R. A. et al. Cloning and characterization of a specific receptor for mouse oncostatin M. *Mol. Cell Biol.* **18**, 3357–3367 (1998).
28. Adrian-Segarra, J. M. et al. The AB loop and D-helix in binding site III of human Oncostatin M (OSM) are required for OSM receptor activation. *J. Biol. Chem.* **293**, 7017–7029 (2018).
29. Boulanger, M. J., Chow, D. C., Brevnova, E. E. & Garcia, K. C. Hexameric structure and assembly of the interleukin-6/IL-6 alpha-receptor/gp130 complex. *Science* **300**, 2101–2104 (2003).
30. Caveney, N. A., Glassman, C. R., Jude, K. M., Tsutsumi, N. & Garcia, K. C. Structure of the IL-27 quaternary receptor signaling complex. *Elife* **11**, e78463 (2022).
31. Jin, Y. et al. Structural insights into the assembly and activation of the IL-27 signaling complex. *EMBO Rep.* **23**, e55450 (2022).
32. Metcalfe, R. D. et al. Structures of the interleukin 11 signalling complex reveal gp130 dynamics and the inhibitory mechanism of a cytokine variant. *Nat. Commun.* **14**, 7543 (2023).
33. Gardner, S. et al. Structural insights into IL-11-mediated signalling and human IL6ST variant-associated immunodeficiency. *Nat. Commun.* **15**, 2071 (2024).
34. Du, Q., Qian, Y. & Xue, W. Molecular Simulation of Oncostatin M and Receptor (OSM-OSMR) Interaction as a Potential Therapeutic Target for Inflammatory Bowel Disease. *Front Mol. Biosci.* **7**, 29 (2020).
35. Du, Q., Qian, Y. & Xue, W. Cross-reactivity of two human IL-6 family cytokines OSM and LIF explored by protein-protein docking and molecular dynamics simulation. *Biochim Biophys. Acta Gen. Subj.* **1865**, 129907 (2021).
36. Olivier, C. et al. Identification of a gp130 cytokine receptor critical site involved in oncostatin M response. *J. Biol. Chem.* **275**, 5648–5656 (2000).
37. Liu, H. et al. Molecular dissection of human oncostatin M-mediated signal transductions through site-directed mutagenesis. *Int J. Mol. Med* **23**, 161–172 (2009).
38. Jumper, J. et al. Highly accurate protein structure prediction with AlphaFold. *Nature* **596**, 583–589 (2021).
39. Boulanger, M. J., Bankovich, A. J., Kortemme, T., Baker, D. & Garcia, K. C. Convergent mechanisms for recognition of divergent cytokines by the shared signaling receptor gp130. *Mol. Cell* **12**, 577–589 (2003).
40. Skiniotis, G., Lupardus, P. J., Martick, M., Walz, T. & Garcia, K. C. Structural organization of a full-length gp130/LIF-R cytokine receptor transmembrane complex. *Mol. Cell* **31**, 737–748 (2008).
41. Huyton, T. et al. An unusual cytokine:Ig-domain interaction revealed in the crystal structure of leukemia inhibitory factor (LIF) in complex with the LIF receptor. *Proc. Natl Acad. Sci. USA* **104**, 12737–12742 (2007).
42. Fischer, M. et al. I. A bioactive designer cytokine for human hematopoietic progenitor cell expansion. *Nat. Biotechnol.* **15**, 142–145 (1997).
43. Skiniotis, G., Boulanger, M. J., Garcia, K. C. & Walz, T. Signaling conformations of the tall cytokine receptor gp130 when in complex with IL-6 and IL-6 receptor. *Nat. Struct. Mol. Biol.* **12**, 545–551 (2005).
44. Kurth, I. et al. Importance of the membrane-proximal extracellular domains for activation of the signal transducer glycoprotein 130. *J. Immunol.* **164**, 273–282 (2000).
45. Timmermann, A., Kuster, A., Kurth, I., Heinrich, P. C. & Muller-Newen, G. A functional role of the membrane-proximal extracellular domains of the signal transducer gp130 in

- heterodimerization with the leukemia inhibitory factor receptor. *Eur. J. Biochem* **269**, 2716–2726 (2002).
46. Mohan, K. et al. Topological control of cytokine receptor signaling induces differential effects in hematopoiesis. *Science* **364**(2019).
47. Punjani, A., Rubinstein, J. L., Fleet, D. J. & Brubaker, M. A. cryoSPARC: algorithms for rapid unsupervised cryo-EM structure determination. *Nat. Methods* **14**, 290–296 (2017).
48. Punjani, A., Zhang, H. & Fleet, D. J. Non-uniform refinement: adaptive regularization improves single-particle cryo-EM reconstruction. *Nat. Methods* **17**, 1214–1221 (2020).
49. Pettersen, E. F. et al. UCSF Chimera—a visualization system for exploratory research and analysis. *J. Comput. Chem.* **25**, 1605–1612 (2004).
50. Emsley, P., Lohkamp, B., Scott, W. G. & Cowtan, K. Features and development of Coot. *Acta Crystallogr. D. Biol. Crystallogr.* **66**, 486–501 (2010).
51. Liebschner, D. et al. Macromolecular structure determination using X-rays, neutrons and electrons: recent developments in Phenix. *Acta Crystallogr. D. Struct. Biol.* **75**, 861–877 (2019).
52. Williams, C. J. et al. MolProbity: More and better reference data for improved all-atom structure validation. *Protein Sci.* **27**, 293–315 (2018).
53. Krissinel, E. & Henrick, K. Inference of macromolecular assemblies from crystalline state. *J. Mol. Biol.* **372**, 774–797 (2007).
54. Johnsson, B., Lofas, S. & Lindquist, G. Immobilization of proteins to a carboxymethyl-dextran-modified gold surface for biospecific interaction analysis in surface plasmon resonance sensors. *Anal. Biochem* **198**, 268–277 (1991).
55. Myszkowski, D. G. Improving biosensor analysis. *J. Mol. Recognit.* **12**, 279–284 (1999).

Acknowledgements

We thank Trudy Ramlall and Luke McGoldrick for providing the detergent solubilized full-length hgp130 protein, Sweta Shah, Aasma Khan, and Kristien Tramaglino for generating STAT3 luciferase reporter cell lines, and Regeneron TP-Protein Development team for purification and analytical characterization of several protein components used in this study. This project has been funded by Regeneron Pharmaceuticals.

Author contributions

Y.Z., P.E.S., M.W.S., W.C.O., and M.C.F. conceptualized the studies. Y.Z. prepared complexes, acquired cryo-EM data, processed data, and built and refined the atomic models. P.E.S., J.C., and J.J. contributed most of the reagents and performed the activity assays. G. E. and A. R. performed

the Biacore experiments. M.W.S., W.C.O., and M.C.F. analyzed data and supervised the project. Y.Z. drafted the manuscript, which was edited and finalized with contributions of all authors.

Competing interests

All authors own options and/or stock of Regeneron. M.W.S. and W.C.O. are officers of Regeneron.

Additional information

Supplementary information The online version contains supplementary material available at <https://doi.org/10.1038/s41467-024-54124-1>.

Correspondence and requests for materials should be addressed to Yi Zhou or Matthew C. Franklin.

Peer review information *Nature Communications* thanks Zhi-Jie Liu, and the other, anonymous, reviewer(s) for their contribution to the peer review of this work. A peer review file is available.

Reprints and permissions information is available at <http://www.nature.com/reprints>

Publisher's note Springer Nature remains neutral with regard to jurisdictional claims in published maps and institutional affiliations.

Open Access This article is licensed under a Creative Commons Attribution-NonCommercial-NoDerivatives 4.0 International License, which permits any non-commercial use, sharing, distribution and reproduction in any medium or format, as long as you give appropriate credit to the original author(s) and the source, provide a link to the Creative Commons licence, and indicate if you modified the licensed material. You do not have permission under this licence to share adapted material derived from this article or parts of it. The images or other third party material in this article are included in the article's Creative Commons licence, unless indicated otherwise in a credit line to the material. If material is not included in the article's Creative Commons licence and your intended use is not permitted by statutory regulation or exceeds the permitted use, you will need to obtain permission directly from the copyright holder. To view a copy of this licence, visit <http://creativecommons.org/licenses/by-nc-nd/4.0/>.

© The Author(s) 2024